AGU PUBLICATIONS

JGR

Journal of Geophysical Research: Space Physics

RESEARCH ARTICLE
10.1002/2015JA021226

Key Points:
- The model reproduces the typical growth phase evolution signatures
- The ballooning instability is favorable at local plasma beta peak
- Breakup arc for an event is mapped to X~−14 R_E near midnight

Correspondence to:
C. Yue,
yuechao@atmos.ucla.edu

Citation:
Yue, C., C.-P. Wang, Y. Nishimura, K. R. Murphy, X. Xing, L. Lyons, M. Henderson, V. Angelopoulos, A. T. Y. Lui, and T. Nagai (2015), Empirical modeling of 3-D force-balanced plasma and magnetic field structures during substorm growth phase, *J. Geophys. Res. Space Physics*, *120*, doi:10.1002/2015JA021226.

Received 19 MAR 2015
Accepted 3 AUG 2015
Accepted article online 6 AUG 2015

Empirical modeling of 3-D force-balanced plasma and magnetic field structures during substorm growth phase

Chao Yue[1], Chih-Ping Wang[1], Yukitoshi Nishimura[1], Kyle R. Murphy[2], Xiaoyan Xing[1], Larry Lyons[1], Michael Henderson[3], Vassilis Angelopoulos[4], A. T. Y. Lui[5], and Tsugunobu Nagai[6]

[1]Department of Atmospheric and Oceanic Sciences, UCLA, Los Angeles, California, USA, [2]NASA Goddard Space Flight Centre, Greenbelt, Maryland, USA, [3]Space Science and Applications, Los Alamos National Laboratory, Los Alamos, New Mexico, USA, [4]Department of Earth and Space Sciences, University of California, Los Angeles, California, USA, [5]Applied Physics Laboratory, Johns Hopkins University, Laurel, Maryland, USA, [6]Earth and Planetary Sciences I2-5, Tokyo Institute of Technology, Tokyo, Japan

Abstract Accurate evaluation of the physical processes during the substorm growth phase, including formation of field-aligned currents (FACs), isotropization by current sheet scattering, instabilities, and ionosphere-magnetosphere connection, relies on knowing the realistic three-dimensional (3-D) magnetic field configuration, which cannot be reliably provided by current available empirical models. We have established a 3-D substorm growth phase magnetic field model, which is uniquely constructed from empirical plasma sheet pressures under the constraint of force balance. We investigated the evolution of model pressure and magnetic field responding to increasing energy loading and their configurations under different solar wind dynamic pressure (P_{SW}) and sunspot number. Our model reproduces the typical growth phase evolution signatures: plasma pressure increases, magnetic field lines become more stretched, current sheet becomes thinner, and the Region 2 FACs are enhanced. The model magnetic fields agree quantitatively well with observed fields. The magnetic field is substantially more stretched under higher P_{SW}, while the dependence on sunspot number is nonlinear and less substantial. By applying our modeling to a substorm event, we found that (1) the equatorward movement of proton aurora during the growth phase is mainly due to continuous stretching of magnetic field lines, (2) the ballooning instability is more favorable during late growth phase around midnight tail where there is a localized plasma beta peak, and (3) the equatorial mapping of the breakup auroral arc is at X~−14 R_E near midnight, coinciding with the location of the maximum growth rate for the ballooning instability.

1. Introduction

Ions and electrons in the nightside magnetosphere, driven by the dawn-to-dusk convection electric field, flow earthward and are energized during the substorm growth phase. As a result, plasma pressure is enhanced and the magnetic field configuration becomes stretched, forming the necessary conditions for the development of a substorm. Determining the physical processes that lead to these plasma and magnetic field configuration changes and the effects of these changes are thus crucial to understanding substorms. Accurate evaluation of these processes relies on knowing the realistic three-dimensional (3-D) magnetic field configuration globally. However, such evaluations cannot be provided with sufficient accuracy or as a function of time during growth phase by currently available empirical magnetic field models, which have been shown [e.g., *McCollough et al.*, 2008] to perform well only in certain areas or under certain geomagnetic conditions. Therefore, the goal of our study is to establish the very first empirical model that is capable of reliably describing the high-fidelity evolution of 3-D force-balanced plasma pressure and magnetic field configurations during the substorm growth phase.

During substorm growth phase, the magnetic field changes to maintain force balance with increasing plasma pressures since the plasma flow is slow [e.g., *Angelopoulos et al.*, 1994; *Wang et al.*, 2009]. The increase of radial plasma pressure gradient $\left(\partial \boldsymbol{P}/\partial r\right)$ causes magnetic field lines to further stretch and enhances the perpendicular currents. On the other hand, the azimuthal pressure gradient $\left(\partial \boldsymbol{P}/\partial \varphi\right)$ causes the field-aligned currents

(FACs) flowing into or out of the ionosphere, which bend magnetic field lines. The coupling between plasma and magnetic field thus plays an essential role in the particle dynamics, magnetosphere-ionosphere coupling, and the physical processes causing substorms.

Previous empirical magnetic field models, such as *Olson and Pfitzer* [1974] and Tsyganenko models [e.g., *Tsyganenko*, 1995, 1996], were established from fitting the model fields to observed magnetic field at different times and locations. Such empirical models have been valuable in providing large-scale fields, but they are not constrained physically by force balance between magnetic field and plasma pressure [*Zaharia and Cheng*, 2003]. Also, separate plasma pressure and magnetic field models that have not been established to be in force balance with each other can lead to spurious results when used in physical studies such as stability analysis [e.g., *Zaharia*, 2008; *Xing and Wolf*, 2007]. This is why it is crucial to include both physical (force balance) and observational constraints in modeling the magnetic field.

Furthermore, where substorm onset starts in the plasma sheet has remained one of the outstanding substorm questions and is critical for differentiating substorm onset models, such as the near-Earth neutral line model [*Baker et al*., 1996; *Shiokawa et al*., 1997; *Angelopoulos et al*., 2008], the current disruption model [*Lui*, 1996], and the more recent proposal of a connection from flow bursts and a near-Earth onset instability [*Nishimura et al*., 2010]. Previous studies have used observations together with magnetic field models to try to solve this issue. For example, *Kubyshkina et al.* [2011] analyzed an isolated substorm on 29 March 2009 with Time History of Events and Macroscale Interactions during Substorms (THEMIS) satellites and ground-based all-sky imagers combined with an adjusted time-varying magnetic field model, and they found the equatorial mapping of substorm breakup to be at a radial distance of ~22 R_E, which is about 10 R_E tailward of the mapped location using the Tsyganenko 96 model. *Sergeev et al.* [2012] used a dynamically adapted magnetospheric model combined with isotropic boundaries observed by low-latitude satellites and found that the most equatorward locations of prebreakup arcs mapped to 8–10 R_E in the plasma sheet. *Jiang et al.* [2012] used field-aligned current and electron spectral measurements in the plasma sheet, FAST overpasses of the preonset arcs, and ground measurements to reach the same conclusion, i.e., that the preonset arcs map in the tail just tailward of the inner edge of the electron plasma sheet at around 8–10 R_E. *Chu et al.* [2015] used a dynamic magnetospheric model with real-time substorm currents from their inversion model [*Chu et al*., 2014] and found that the flows at 9–10 R_E mapped to breakup arcs both at expansion phase onset and during the late expansion phase and recovery. Moreover, the growth phase arcs typically do not remain fixed at a given magnetic latitude but move equatorward during the course of the growth phase. If the *Chu et al.*'s results (applicable to expansion and recovery) are any indication, the model differences, mapping uncertainties, and the auroral motions during growth phase may also reflect the lack of a realistic magnetic field model designed for the substorm growth phase. A solution to this issue would be to determine onset location in the plasma sheet through mapping of initial auroral brightening via a realistic magnetic field model for the substorm growth phase.

In addition, ballooning/interchange instability [*Cheng and Qian*, 1994; *Cheng and Lui*, 1998] has been suggested as a plausible mechanism for initiation of substorm onset in the high-β plasma sheet [*Lee and Wolf*, 1992; *Hurricane*, 1997; *Cheng and Lui*, 1998]. Thus, determining the location in the tail plasma sheet where the ballooning instability may initiate is important to understanding the onset. Since the ballooning instability is determined by the plasma and magnetic field spatial variations, accurate evaluation of the ballooning instability requires a realistic 3-D force-balanced plasma pressure distributions and magnetic field configurations.

Understanding and quantifying magnetic field mapping between the ionosphere and the equatorial magnetosphere has long been an important goal of space physics research. In this study, we first establish a realistic 3-D substorm growth phase magnetic field model in section 2 (adopted from *Zaharia* [2008]) that satisfies the physical constraint of force balance with plasma sheet pressures predicted by an empirical model we developed previously [*Yue et al*., 2015]. The uniqueness of our modeling is that the magnetic field is computed solely from plasma pressure distributions and magnetic field observations are only used to validate the model magnetic fields. In section 3, we present our model results under general growth phase conditions and investigate the evolution of 3-D plasma sheet pressure distributions and magnetic field configurations, as well as the current system, during the substorm growth phase to demonstrate that our model can qualitatively reproduce the typical substorm growth phase features. In section 4, we evaluate quantitatively the model accuracy by comparing model results with observations within the plasma sheet. In section 5, we

present the FACs computed from our force-balanced magnetic field and compare our model FACs with observed FACs derived from Active Magnetosphere and Planetary Electrodynamics Response Experiment (AMPERE) for a substorm event. We also briefly discuss plasma pressure and magnetic field responses to different solar wind dynamic pressure (P_{sw}) and sunspot number. By applying our magnetic field model to a substorm event in section 6, we evaluate the dynamics of proton aurora due to current sheet scattering by comparing the magnetospheric ion isotropic boundaries (IBs) with proton auroral observations [e.g., *Ganushkina et al.*, 2005; *Shevchenko et al.*, 2010; *Yue et al.*, 2014], we examine ballooning stability of the plasma sheet configurations, and we determine the onset location in the plasma sheet by using our model to map the ionospheric onset location.

2. Magnetic Field Modeling and Observational Data

A first principle calculation of magnetospheric equilibrium with prescribed initial and boundary conditions can be utilized to study the specific magnetic field configurations during the growth phase as quasistatic equilibrium (the magnetic field satisfies force balance with plasma pressure) is valid [*Voigt and Wolf*, 1988]. *Zaharia* [2008] developed a 3-D force-balanced magnetic field solver by solving the single-fluid force balance equation $\mathbf{J}\times\mathbf{B} = \nabla\cdot\overleftrightarrow{\mathbf{P}}$ in terms of Euler potentials with any specified $\overleftrightarrow{\mathbf{P}}$ distribution. In this study, we combine this magnetic field solver with the empirical substorm growth phase plasma pressure model developed by *Yue et al.* [2015] to model the evolution of the 3-D force-balanced plasma and magnetic field configuration, and the westward current and FACs, as the substorm growth phase develops.

Here we briefly describe the framework of our 3-D empirical force-balanced pressure and magnetic field modeling (see *Yue et al.* [2013, 2015] for more details). Previously, we established a 2-D equatorial plasma sheet pressure model during the substorm growth phase [*Yue et al.*, 2015] using the Support Vector Regression Machine with three primary control parameters: (1) PCPAE energy loading (a loading index considering both the loading from the solar wind and effect from the previous substorm; see *Yue et al.* [2015] for the definition), a quantity that represents the energy state in the plasma sheet during the substorm growth phase; (2) P_{sw}; and (3) the observed monthly average sunspot number. This empirical plasma sheet pressure model is established from Geotail (1995–2005) and THEMIS (2007–2011) observations during substorm growth phase. The model gives plasma sheet pressure as a function of (X, Y) position in the equatorial plane, with P_{sw}, PCPAE loading, and sunspot number as input parameters.

The force-balanced magnetic field is computed from the 3-D magnetic field model by solving the force balance equation $\mathbf{J}\times\mathbf{B} = \nabla\cdot\mathbf{P}$, where $\mathbf{P}$ is the plasma sheet pressure distributions and $\mathbf{B}$ is given by two Euler potentials, $B = \nabla\alpha\times\nabla\beta$. The pressure is assumed to be isotropic in this study, so plasma pressure is constant along field lines. With the Euler potentials, we decoupled the 3-D force balance equation into two coupled 2-D equations in the directions parallel to ($B\times\nabla\alpha$) and ($B\times\nabla\beta$), respectively, as follows:

$$J\cdot\nabla\alpha = \nabla\cdot\left[(\nabla\alpha)^2\nabla\beta - (\nabla\alpha\cdot\nabla\beta)\nabla\alpha\right] = -\frac{\partial P}{\partial\beta} \tag{1}$$

$$J\cdot\nabla\beta = \nabla\cdot\left[(\nabla\beta\cdot\nabla\alpha)\nabla\beta - (\nabla\beta)^2\nabla\alpha\right] = \frac{\partial P}{\partial\alpha} \tag{2}$$

The constant α and β surfaces are obtained by solving equations (1) and (2) numerically. In this study, the model outer boundary conditions, which are the values of α, β, and the inhomogeneous terms on the right-hand sides $\left(\frac{\partial P}{\partial\alpha}\right.$ and $\left.\frac{\partial P}{\partial\beta}\right)$, are prescribed, respectively, with values from the Tsyganenko 89 (T89) model and the growth phase pressure model. Here we set the inner boundary at $r = 2\ R_E$ and assume dipole field inside 2 R_E. The shape of the outer boundary location in the equatorial plane is a prescribed ellipse with the Earth as one of the foci. The farthest point is $X = 6\ R_E$ on the dayside and $X = -20\ R_E$ on the nightside. After setting up the model boundary, the only input to our 3-D force-balanced magnetic field model is the 2-D equatorial plasma sheet pressure distributions obtained from the 2-D empirical plasma sheet pressure model developed in *Yue et al.* [2015]. The outputs are 3-D magnetic field configurations, plasma pressure distributions (pressure is constant along the field lines since we assume isotropic pressure), and current density.

To evaluate quantitatively how accurate our model magnetic fields are in section 4, we use the magnetic field observations obtained from Geotail and THEMIS spacecraft; same data were used to establish the 2-D

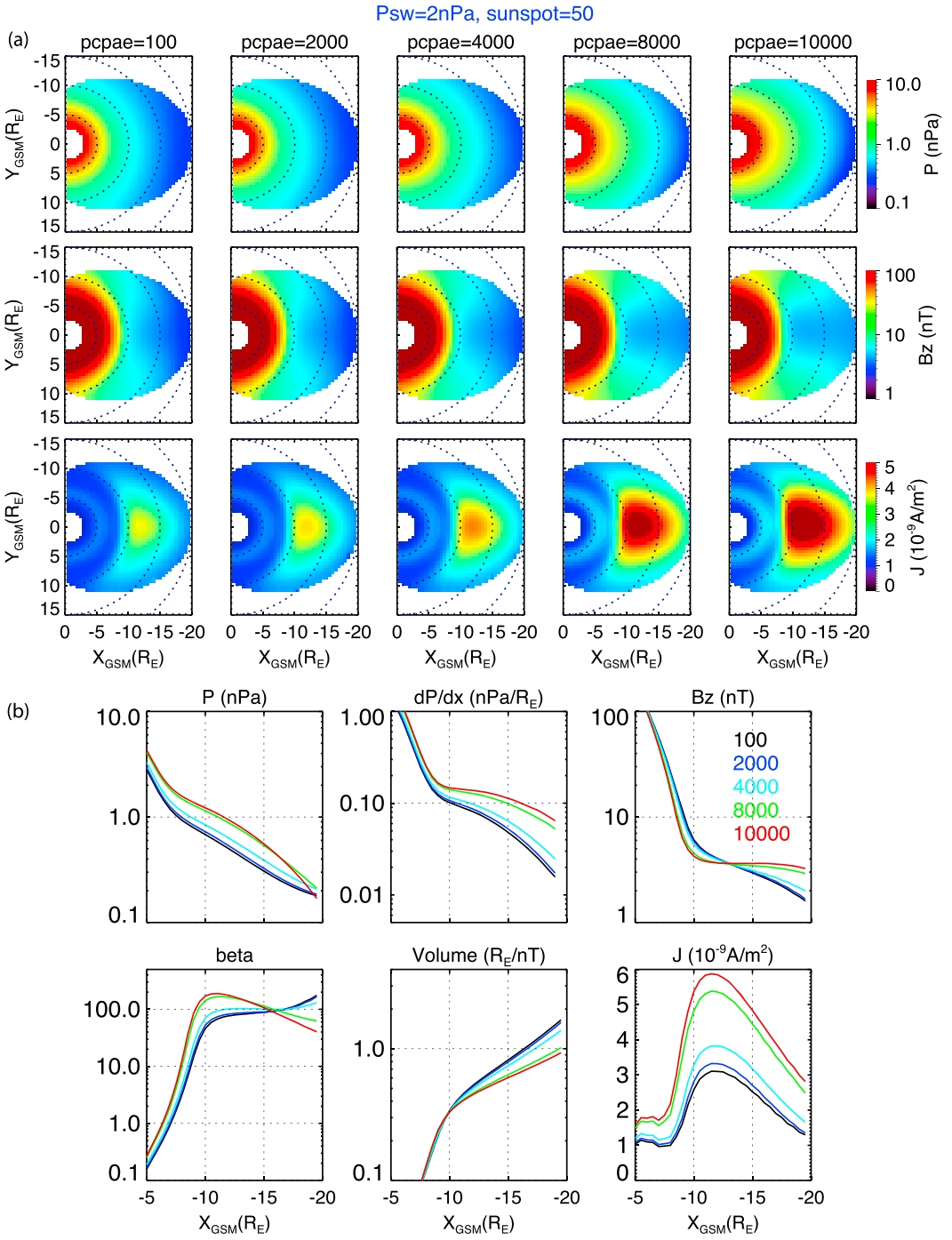

Figure 1. (a) The equatorial distributions of modeled pressure, B_z, and westward J_φ for five different PCPAE loading (100, 2000, 4000, 8000, and 10,000 kV min) with P_{sw} = 2 nPa and sunspot = 50 to demonstrate the substorm growth phase development. (b) The midnight radial profile of equatorial plasma pressure, plasma pressure gradient, B_z, plasma beta, flux tube volume per unit flux from the equatorial plane to the ionosphere, and westward J_φ for the same control parameters as Figure 1a. The black, blue, light blue, green, and red lines are for PCPAE loading = 100, 2000, 4000, 8000, and 10,000, respectively.

empirical plasma sheet pressure model (see *Yue et al.* [2015] for more details about the observed magnetic field database). To evaluate our FAC results for a substorm event in section 5.1, we use the global FAC patterns in the ionosphere derived from the Active Magnetosphere and Planetary Electrodynamics Response Experiment (AMPERE), which are inferred from the magnetic field measured on the Iridium constellation of low-Earth orbiting (781 km) satellites [*Anderson et al.*, 2000; *Waters et al.*, 2001]. For the one substorm

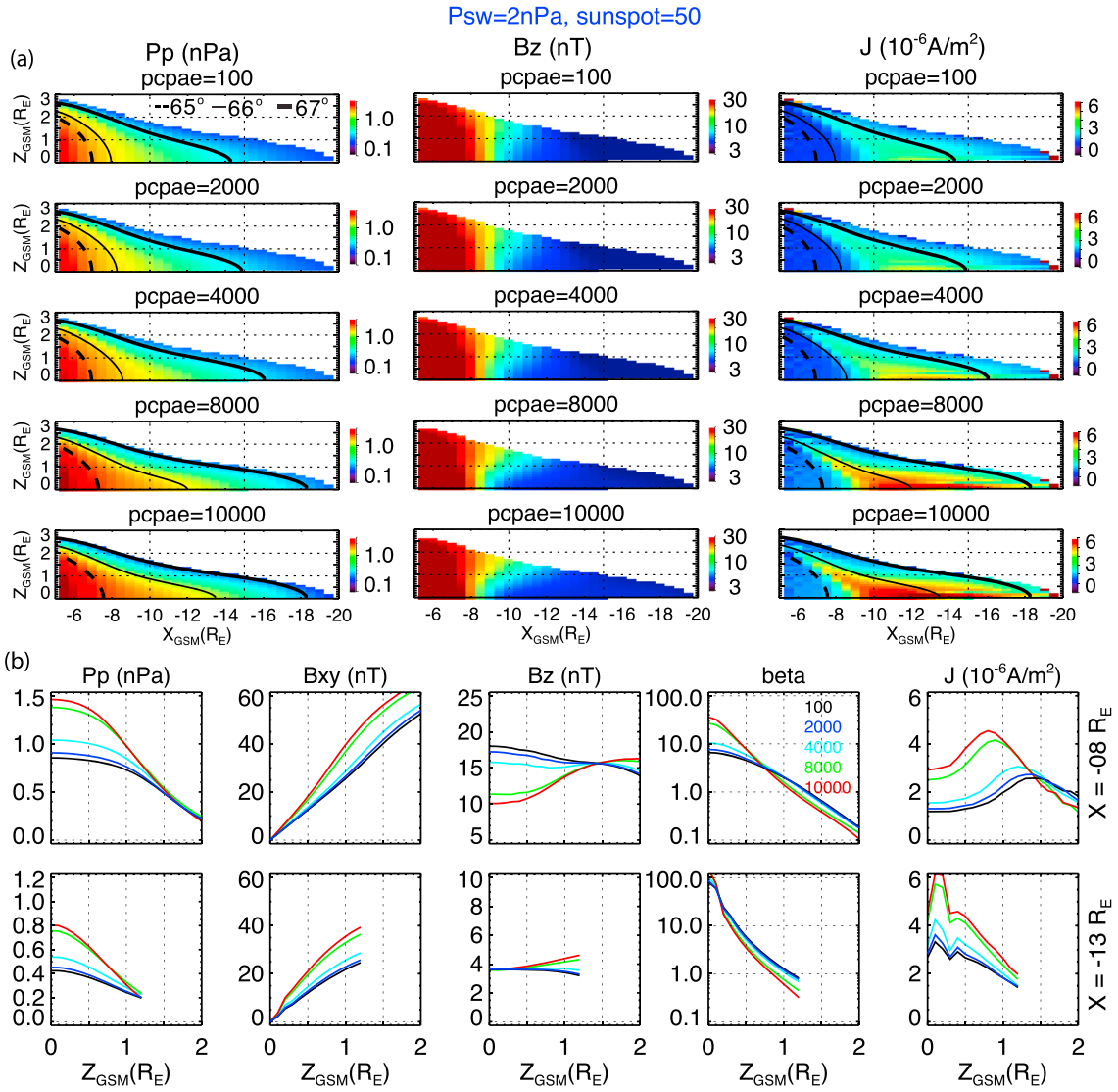

Figure 2. (a) The midnight *X-Z* plane distributions of modeled pressure, B_z, and westward J_φ for five different PCPAE loadings (100, 2000, 4000, 8000, and 10,000 kV min) with $P_{sw} = 2$ nPa and sunspot = 50 to demonstrate the substorm growth phase development. The black curves are the magnetic field lines from three different latitudes. (b) The *Z* radial profile of plasma pressure, B_{xy}, B_z, plasma beta, and westward J_φ at $Y = 0$ and $X = -8$ and -13 R_E for the same control parameters as Figure 2a. The black, blue, light blue, green, and red lines are for PCPAE loading = 100, 2000, 4000, 8000, and 10,000, respectively.

event study presented in section 6, THEMIS ground-based all-sky imagers [*Donovan et al.*, 2006] are used to show that the aurora dynamics and the observed magnetic field from magnetometers on GOES [*Singer et al.*, 1996] and Fluxgate Magnetometer instrument [*Auster et al.*, 2008] on board THEMIS are used to compare with the model magnetic field.

3. Model Results: Evolution of Substorm Growth Phase—Energy Loading Effect

In this section, we examine the growth phase evolution of pressure, magnetic field, and current density profile in the equatorial plane and along the midnight meridian corresponding to increasing PCPAE loading under constant P_{sw} and sunspot number to demonstrate whether our physical-based self-consistent model can qualitatively reproduce the typical signatures of a substorm growth phase. In the next session, we evaluate quantitatively the accuracy of our model substorm growth evolution by comparing with observations.

Figure 1 shows the equatorial plasma pressure, magnetic field, and westward currents for five different energy loading values (100, 2000, 4000, 8000, and 10,000 kV min) with $P_{sw} = 2$ nPa and sunspot number = 50.

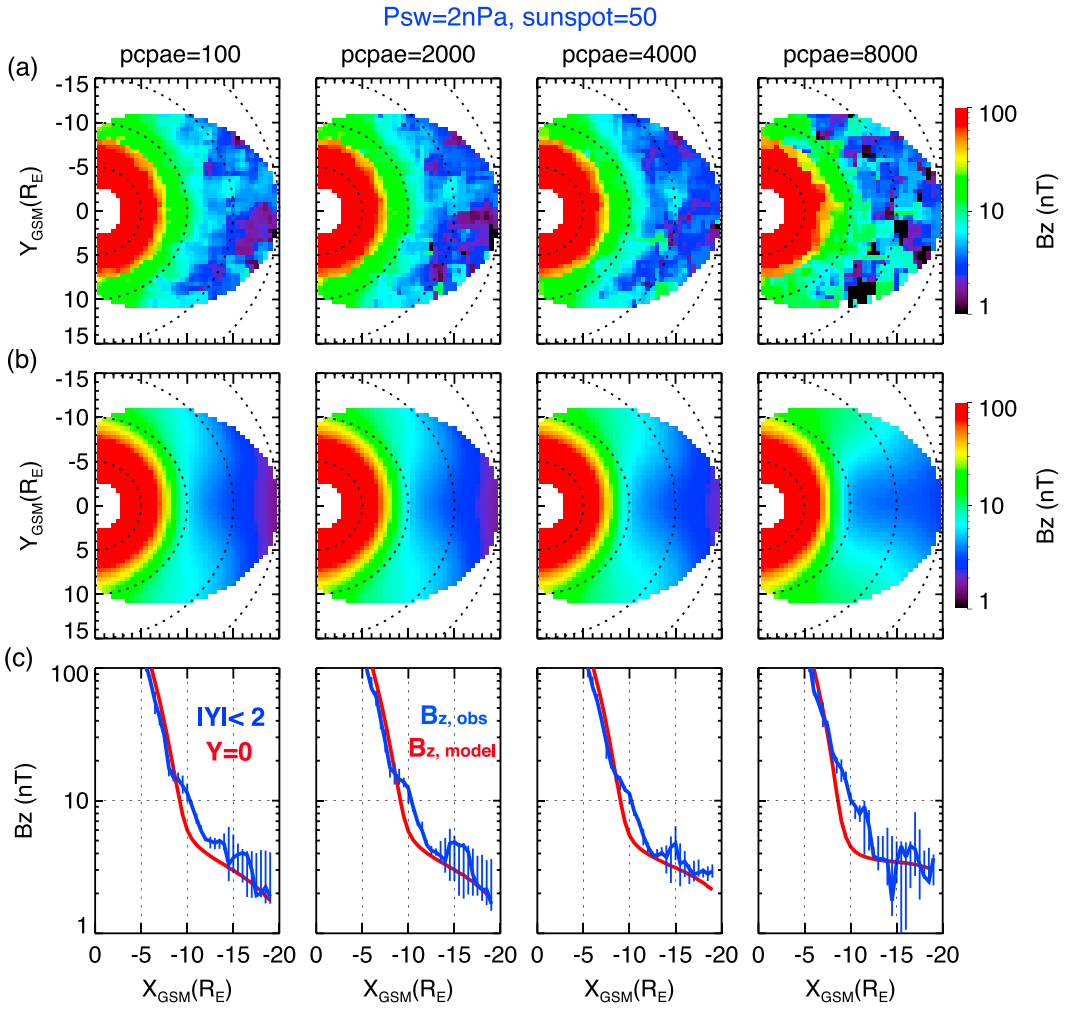

Figure 3. Equatorial distributions of (a) observed B_z and (b) model force-balanced B_z. (c) Comparisons of the radial profiles of observed B_z (the blue curves) and the model B_z (the red curves) near the midnight MLT for four different PCPAE loadings (100, 2000, 4000, and 8000 kV min) with $P_{sw} = 2$ nPa and sunspot = 50.

These loading values are chosen to represent the increasing loading typically seen for a strong substorm (*AE* max > 600 nT [see *Yue et al.*, 2015]), with PCPAE = 100 corresponding to the beginning of the growth phase and 10,000 to just before substorm onset. Figure 1a shows that the plasma pressure gradually increases as energy loading increases with no significant dawn-dusk asymmetry, while B_z gradually increases in the magnetotail with smaller value at midnight than near the flanks and the westward current (J_φ) gradually increases and peaks around midnight. Along the midnight meridian as shown in Figure 1b, the plasma pressure and its gradient increase, while magnetic flux tube volume decreases, as energy loading increases. B_z increases in the tail but decreases in the inner magnetosphere due to the increasing J_φ as energy loading increases. Plasma beta shows a peak forming during the late growth phase around 11 R_E. The flat B_z profile within the high-β plasma sheet during the late growth phase could be the favorable condition for plasma sheet instabilities, such as ballooning/interchange instabilities, which may initiate substorm onset. This is further discussed in section 6.

Figure 2 shows the model results in the midnight meridian plane and the variations with Z at $X = -8$ and -13 R_E. It is shown that plasma pressure increases as energy loading increases along the midnight meridian in Figure 2a. As a result, the field lines from three fixed latitudes (65°, 66°, and 67°) become more stretched and map to further down the tail. B_z shows a positive gradient in the Z direction (dBz/dZ > 0) in the vicinity of $X = -10$ R_E, and the area of positive dBz/dZ becomes larger as energy loading increases. In addition, the westward J_φ increases as energy loading increases, and its contour is aligned approximately with field lines, which is a feature resulting from force balance that other empirical models do not take into account.

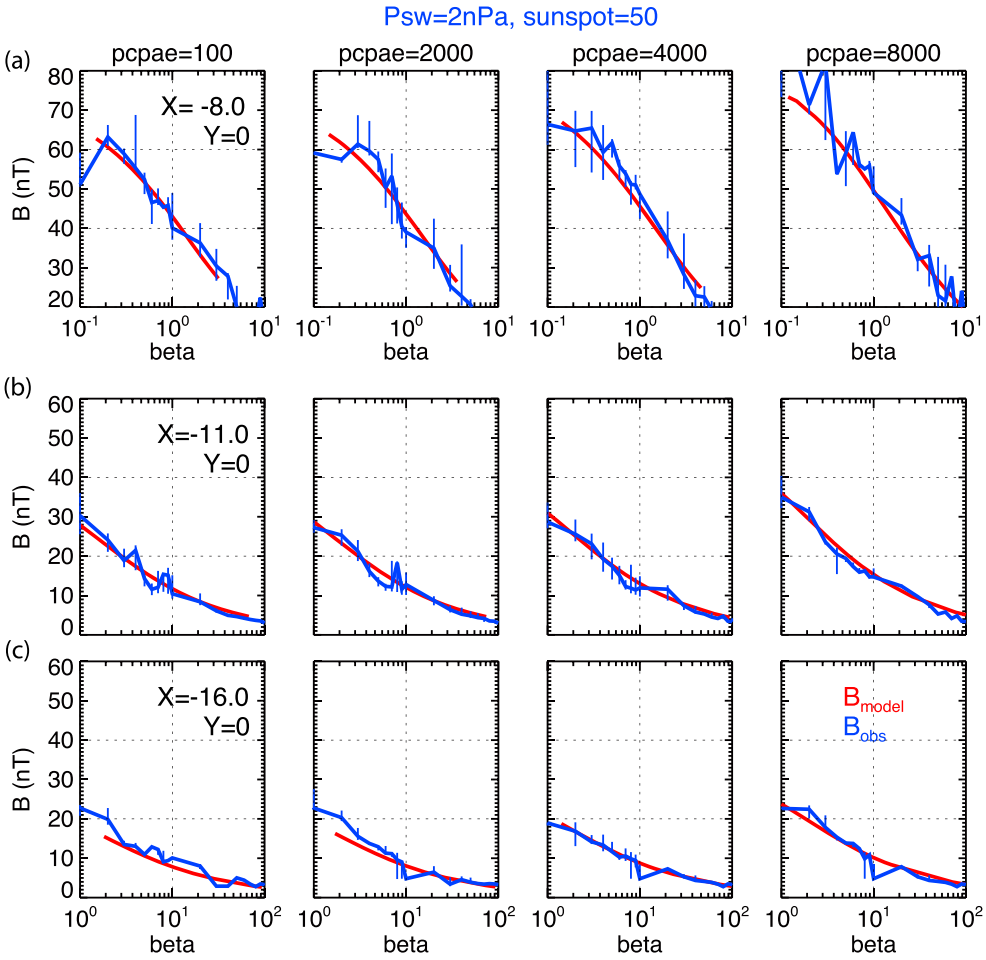

Figure 4. Total magnetic field as a function of plasma beta at (a) $X = -8$, $Y = 0$ R_E and (b) $X = -11$, $Y = 0$ R_E. (c) $X = -16$, $Y = 0$ R_E of the observed (the blue curves) and model magnetic field (the red curves) for four different PCPAE loadings (100, 2000, 4000, and 8000 kV min) with $P_{sw} = 2$ nPa and sunspot = 50.

Along the Z direction shown in Figure 2b, plasma pressure and B_{xy} increase as energy loading increases while B_z decreases at the equator but increases off the equator during the late growth phase, showing positive dBz/dz (as seen by the green and red curves in the third column in Figure 2b) at both locations ($X = -8$ and -13 R_E). It is interesting to note that the positive dBz/dz signature has been observed by THEMIS [*Saito et al.*, 2010, 2011]. However, a corresponding local equatorial B_z minimum as a function of radial distance predicted by *Saito et al.* is not seen in our model results. Additionally, J_φ peaks off the equatorial plane in the near-Earth region, and the Z locations of the peak move toward the equatorial plane as energy loading increases, indicating that the current sheet is thinning as the growth phase develops.

4. Model Evaluation

Our model results above show the typical picture of plasma sheet dynamics during the substorm growth phase: plasma pressure increases, magnetic field lines become more stretched, westward current is enhanced, and current sheet thins. To evaluate quantitatively how reliable our model results are, we compare the model B_z on the equatorial plane and total magnetic field strength along the Z direction with the observed magnetic fields obtained from the Geotail and THEMIS satellites for PCPAE loading = 100, 2000, 4000, and 8000 kV min with $P_{sw} = 2$ nPa and sunspot number = 50 in Figures 3 and 4. Figures 3a and 3b show comparisons between the observed and modeled B_z at the equatorial plane. We have selected the observed B_z near the equatorial region with the plasma beta > 2. As shown in Figure 3a, the observed B_z in the plasma sheet increases with increasing PCPAE loading with values relatively smaller near midnight than flank region.

The model B_z in Figure 3b matches reasonably well the observations in the large-scale spatial distributions and its response to PCPAE loading, although the observed B_z for PCPAE = 8000 is more scattered than for the lower PCPAE values. Figure 3c shows that the model B_z (red lines) in the plasma sheet agrees generally well with observed B_z (blue lines with the errors bar indicating the 25% and 75% quartiles). The modeled B_z has lower magnitudes than the observations from ~9 to 12 R_E, a difference that could be due to the model B_z being evaluated strictly at $Z = 0$, while the observations include data points in the vicinity of the equatorial plane. As shown in Figure 2a, B_z actually becomes higher as Z increases at r~8 to 12 R_E, thus likely leading to higher B_z values than would be obtained if we were able to obtain observations strictly at the equator.

To evaluate the model magnetic field variations along the Z direction, we plot in Figure 4 the total model magnetic field strengths as a function of plasma beta (red curves) in comparison with the median values of observed strengths (blue lines with the errors bar indicating the 25% and 75% quartiles) at three different radial distances ($r = 8$, 11, and 16 R_E). Here we use plasma beta to represent Z variations since plasma beta decreases with increasing Z, and it is impossible to determine the exact observed Z location relative to the equatorial plane. Figure 4 shows that the model agrees very well with the observed field magnitudes and variations with beta and the responses to energy loading at all radial distances.

5. Discussion

5.1. Field-Aligned Currents

The equatorial mapping of integrated FAC density $J_{||}$ in the ionosphere for five different energy loadings with $P_{sw} = 2$ nPa and sunspot number = 50 is shown in Figure 5. FACs are computed using the Vasyliunas equation [*Vasyliunas*, 1970, 1984] $\frac{J_{||}}{B_{iono}} = \frac{\mathbf{B}_{eq}}{B_{eq}^2} \cdot \left(\Delta V \times \Delta P_{eq}\right)$. At the beginning of growth phase, there are typical Region 1 (R1) FACs in the tail with upward (downward) FACs at the premidnight (postmidnight) magnetic local times (MLTs). There is a small upward Region 2 (R2) FAC in the postmidnight close to the Earth. As the energy loading increases, the R2 FACs intensify and extend both earthward and tailward, while the R1 FACs retreat tailward. As shown in Figure 1, as the energy loading increases, the plasma pressure increases more strongly near midnight while B_z increases more strongly near the flanks, resulting in more enhanced azimuthal current density near midnight than the flanks and thus intensified R2 FACs to main current continuity. At the late growth phase, the typical R2 FACs develop with downward (upward) FACs at premidnight (postmidnight) MLTs, and the R1 FACs disappear from the field of view.

To evaluate our FACs, we compare with the FACs derived from AMPERE (details about how to derive the FACs from AMPERE can be found in *Murphy et al.* [2012]). Since a statistical pattern of AMPERE FACs for the substorm growth phase has not been established, we did an initial check using a substorm event on 7 March 2010 (onset time is 05:17 UT), which has very good spatial coverage of magnetic field data for deriving FACs from AMPERE. To model FACs for this event, we first obtained the 2-D equatorial pressure profile for different times of the growth phase from our 2-D empirical plasma sheet pressure model by using the observed temporal profiles of P_{sw} and PCPAE loading as input (the observed monthly averaged sunspot number was 15.3). We then computed the force-balanced magnetic field and associated FACs.

Figures 5b and 5c show comparison between the AMPERE FACs (the red and blue colors indicate downward and upward FACs into and from the ionosphere, respectively) during 04:34–04:44 and 04:48–04:58 UT and model FACs at 04:38 and 04:53 UT. The gray color in Figure 5b indicates the very weak FACs (less than 0.1 $\mu A/m^2$). It can be seen that during 04:34–04:44 UT, there are observed upward FACs at high latitudes (~68°–70°) in the premidnight sector and a pair of Region 2 sense FACs with downward (upward) FACs at premidnight (postmidnight) at low latitudes (~64°–66°). The observed FACs intensify (04:48–04:58 UT) as the substorm growth phase develops, showing typical Region 1 sense FACs at the high latitudes (~67°–70°) and Region 2 sense FACs at the low latitudes (~63°–66°). The model FAC patterns match reasonably well with the observations despite some discrepancies in the latitude and magnitude. Comparing Figures 5b and 5c shows that the observed FACs spread more broadly over latitude than do the model FACs. The larger spread of the observed FACs may be due to the 10 min averaging interval of the data, during which the magnetic field stretches causing the ionospheric latitudes of the FACs to change. In addition, the AMPERE FACs are computed using 20 s magnetometer data along six orbital planes which are mapped to a corrected geomagnetic and magnetic local time grid with a resolution of 1° and 1 h of MLT at 10 min intervals (the time required

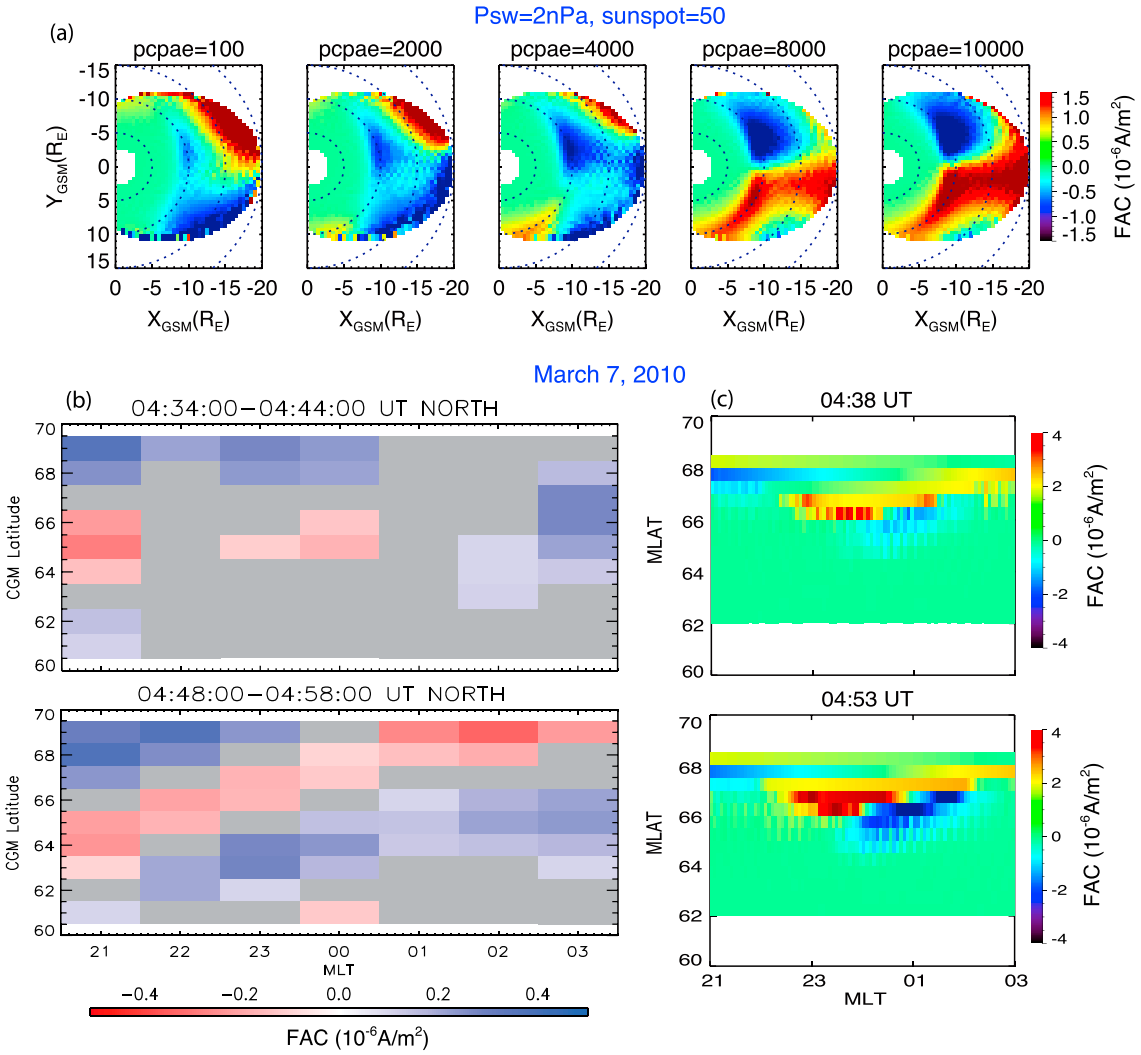

Figure 5. (a) The equatorial field-aligned currents distributions for five different PCPAE loadings (100, 2000, 4000, 8000, and 10,000 kV min) with P_{sw} = 2 nPa and sunspot = 50. (b) The derived AMPERE FACs (red, downward and blue, upward) in ionosphere as functions of magnetic latitude (MLAT) and MLT during 04:34–04:44 and 04:48–04:58 UT quasi-stationary time periods for 7 March 2010 substorm event (onset occurred at 05:17 UT according to auroral observations). (c) Model ionospheric FACs (red, downward and blue, upward) distributions as functions of MLAT and MLT at 04:38 and 04:53 UT.

to collect data throughout the northern hemisphere). The 20 s resolution of the AMPERE magnetometers and subsequent 10 min gridding will tend to smooth the AMPERE FACs. This smoothing of the AMPERE FACs along with the higher spatial and temporal resolution with which the model FACs are computed, such that spatially and temporally localized currents can be resolved, will contribute to the difference in the amplitude between the modeled and derived AMPERE FACs.

5.2. Effect of P_{sw} and Sunspot Number

While the growth phase pressure and magnetic field mainly respond to the increasing PCPAE loading, these responses also depend on P_{sw} and sunspot number, which can be quite different for each substorm. Here we briefly describe the dependencies on these two factors. Figures 6 and 7 show the model results on the equatorial plane and along the midnight meridian, respectively, corresponding to the same PCPAE loading (4000 kV min) but to different values of P_{sw} (2 and 4 nPa) and sunspot number (20 and 50) as labeled on top of each column. From Figure 6a, when the sunspot number is higher, the plasma pressure is higher in the inner magnetosphere but becomes lower in the tail, resulting in stronger pressure gradient, enhanced westward current, and substantial increase of B_z in the tail. Note that the dependence on sunspot number is not linear. Pressure increases with increasing sunspot number until ~60–80 then decreases again

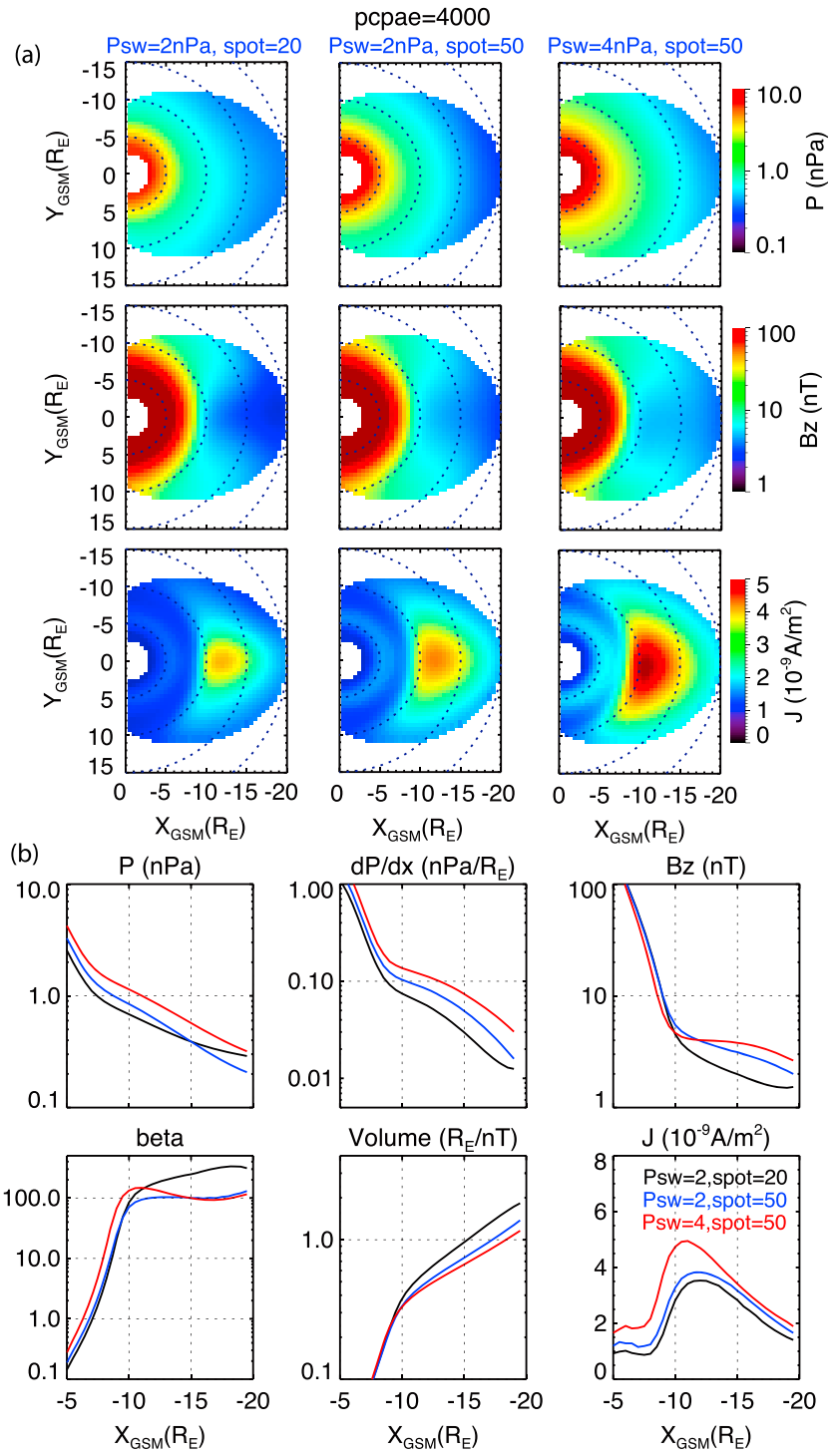

Figure 6. (a) The equatorial distributions of modeled pressure, B_z, and westward J_φ for PCPAE loading = 4000 kV min with P_{sw} = 2 nPa, sunspot = 20; P_{sw} = 2 nPa, sunspot = 50; P_{sw} = 4 nPa, sunspot = 50 to illustrate the effects of P_{sw} and sunspot number. (b) The midnight radial profile of equatorial plasma pressure, plasma pressure gradient, B_z, plasma beta, flux tube volume per unit flux from the equatorial plane to the ionosphere, and westward J_φ for the same control parameters as Figure 6a. The black, blue, and red lines are for P_{sw} = 2 nPa, sunspot = 20; P_{sw} = 2 nPa, sunspot = 50; P_{sw} = 4 nPa, sunspot = 50, respectively.

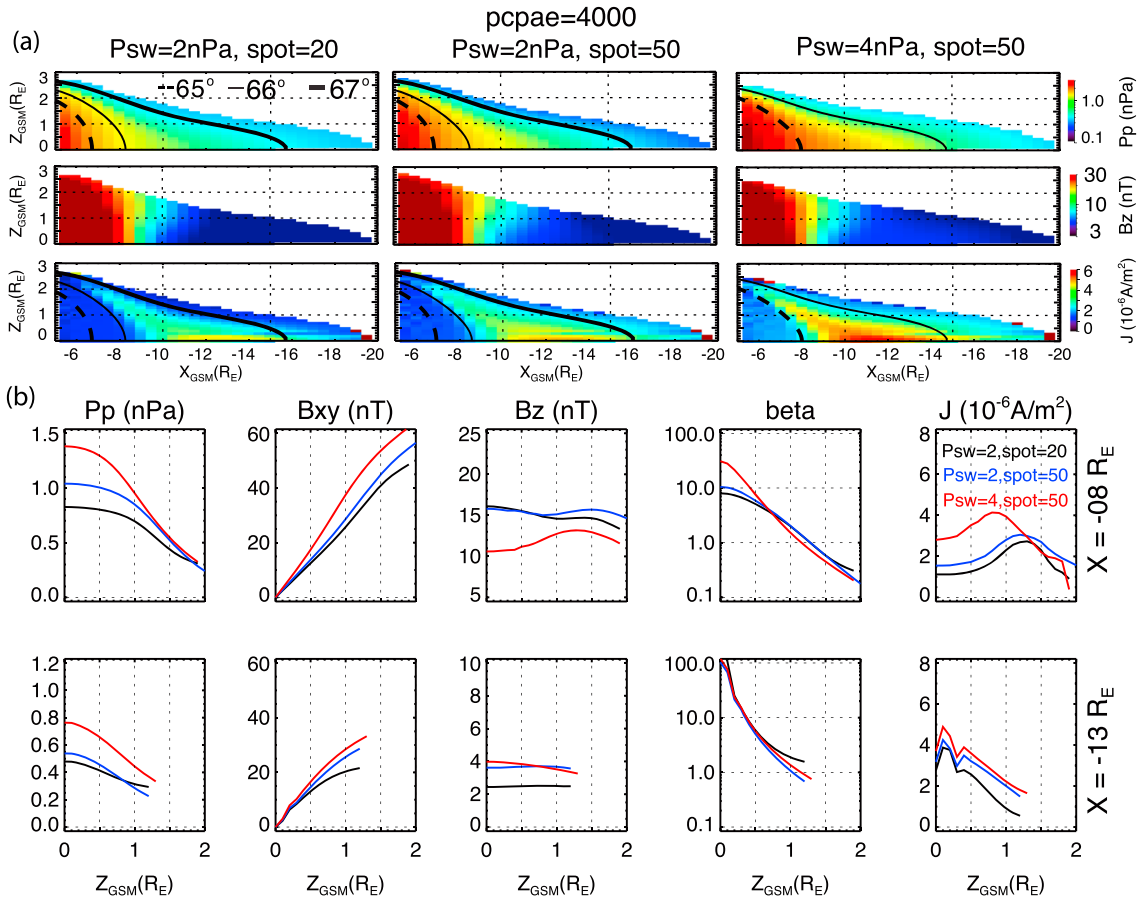

Figure 7. (a) The midnight *X-Z* plane distributions of modeled pressure, B_z, and westward J_φ for PCPAE loading = 4000 kV min with P_{sw} = 2 nPa, sunspot = 20; P_{sw} = 2 nPa, sunspot = 50; P_{sw} = 4 nPa, sunspot = 50 to illustrate the effects of P_{sw} and sunspot number. The black curves are the magnetic field lines from three different latitudes. (b) The *Z* radial profile of plasma pressure, B_{xy}, B_z, plasma beta, and westward J_φ at $Y = 0$ and $X = -8$ and -13 R_E for the same control parameters as Figure 7a. The black, blue, and red lines are for P_{sw} = 2 nPa, sunspot = 20; P_{sw} = 2 nPa, sunspot = 50; P_{sw} = 4 nPa, sunspot = 50, respectively.

(see *Yue et al.* [2015] for possible explanation of the nonlinear dependence). As P_{sw} increases, the plasma pressure and pressure gradient increase and magnetic field B_z decreases in the near-Earth region but increases in the tail due to the increasing westward current J_φ and the J_φ peak moving earthward. The response to P_{sw} may be a result of the balance between P_{sw} and magnetosphere pressure (magnetic pressure in the lobes and plasma pressure on the equatorial plane) as discussed in *Yue et al.* [2013, 2015].

As shown in Figure 7, while the magnitudes of pressure, magnetic fields, and current density change with changing P_{sw} and sunspot number, the *X-Z* profiles of these parameters remain similar. The magnetic field configurations are slightly more stretched when sunspot number changes from 20 to 50 but are significantly more stretched when P_{sw} increases from 2 to 4 nPa as indicated by the field lines for the three fixed latitudes (65°, 66°, and 67°).

6. Model Application: A Substorm Event Study

Since the evaluation shown above indicates that our model gives a good statistical description of the substorm growth phase, we have applied the model to a substorm event to analyze the physical processes associated with the evolution of the plasma and magnetic field, including the evolution of proton aurora due to current sheet scattering, ballooning instability, and the substorm onset location in the plasma sheet. Here we show an example of our analysis of a substorm event on 5 March 2008. As can be seen from the aurora observed by 630.0 and 486.1 nm wavelengths of the NORthern Solar Terrestrial ARray meridian scanning photometers at Gillam station (located at ~23.4 MLT at the onset) shown in Figures 8a and 8b, both the electron and proton aurora moved equatorward during the growth phase and the electron aurora breakup

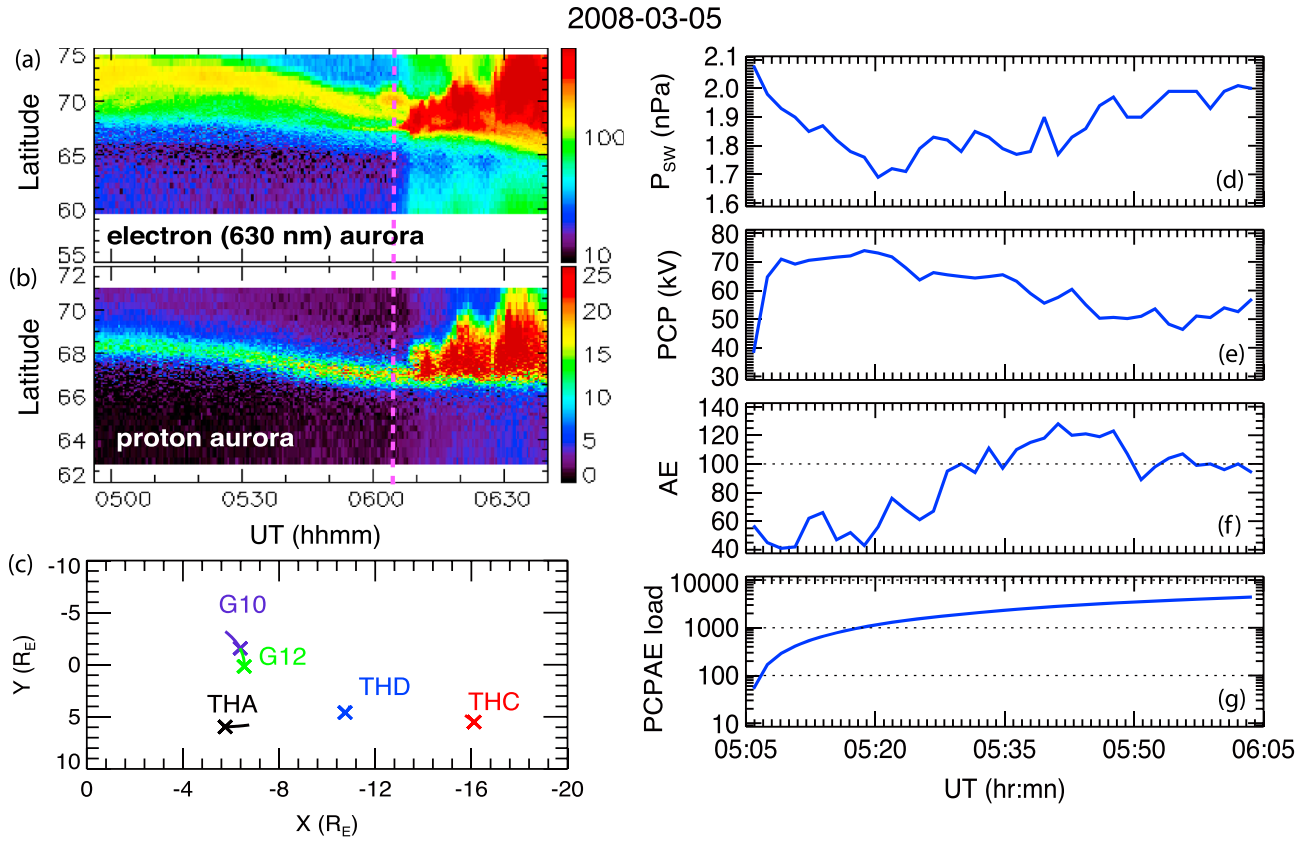

Figure 8. The overview of 5 March 2008 substorm event. (a and b) Electron and proton aurora observed by Gillam station around midnight meridian. The vertical dashed line marks the substorm onset time 06:04 UT according to electron aurora observation. (c) THEMIS A, C, and D and GOES 10 and GOES 12 trajectories at *X-Y* plane in GSM coordinates during substorm growth phase. The black, blue, and red lines are the THEMIS A, D, and C, while the purple and green lines are the GOES 10 and GOES 12, respectively. (d–g) The variation of P_{sw}, CPCP, *AE*, and the PCPAE loading based on OMNI data during 05:05–06:05 UT.

started at 67.3° latitude at 06:04 UT followed by poleward expansion of aurora. The electron aurora breakup arc is located at the poleward shoulder of the proton aurora, as is typically observed [*Donovan et al.*, 2012]. As shown in Figure 8c, this event is chosen for having good spatial coverage of the nightside plasma sheet by two geosynchronous satellites (GOES 10 and GOES 12) very near midnight and three THEMIS satellites radially aligned (TH-A, TH-D, and TH-C at X_{GSM}~6, 11, and 16 R_E, respectively) at Y_{GSM}~5 R_E, thus providing excellent coverage for evaluation of our model predictions. Figures 8d–8f show that during the growth phase P_{sw} varied slightly between 1.7 and 2 nPa, PCP gradually decreased from 70 to 50 kV, and *AE* slowly increased from 40 to ~100 nT. The *AE* during the growth phase was small and then reached ~400 nT after the onset (not shown), indicating that this is an isolated and moderate substorm. The computed PCPAE loading, shown in Figure 8g, increased from ~50 to 5000 kV min.

Using the observed P_{sw} and PCPAE loading shown in Figures 8d and 8g and the observed monthly averaged sunspot number of 9.3 for this event, we predict the evolution of the plasma sheet pressure and magnetic field. Figure 9 shows the comparison between modeled results and observations. The black and blue lines in Figure 9a are plasma and total pressures observed by THEMIS, respectively, and the red lines are the model equatorial pressures. As shown in Figure 8c, TH-A moved tailward in the inner magnetosphere from around r~6 R_E and remained close to the central plasma sheet since the total pressure is similar to the plasma pressure throughout the growth phase in Figure 9a. TH-D was at r~11 R_E while TH-C was at r~16 R_E, and both were moving eastward and moving away from the central plasma sheet as indicated by the plasma pressure becoming smaller than the total pressure. This is likely due to the magnetic field becoming more stretched and the plasma sheet becoming thinner as the growth phase develops. The model pressures match reasonably well with observed total pressure in general, except for TH-D from ~20 min prior to the onset, when TH-D became far away from the current sheet where the pressure model prediction becomes less reliable.

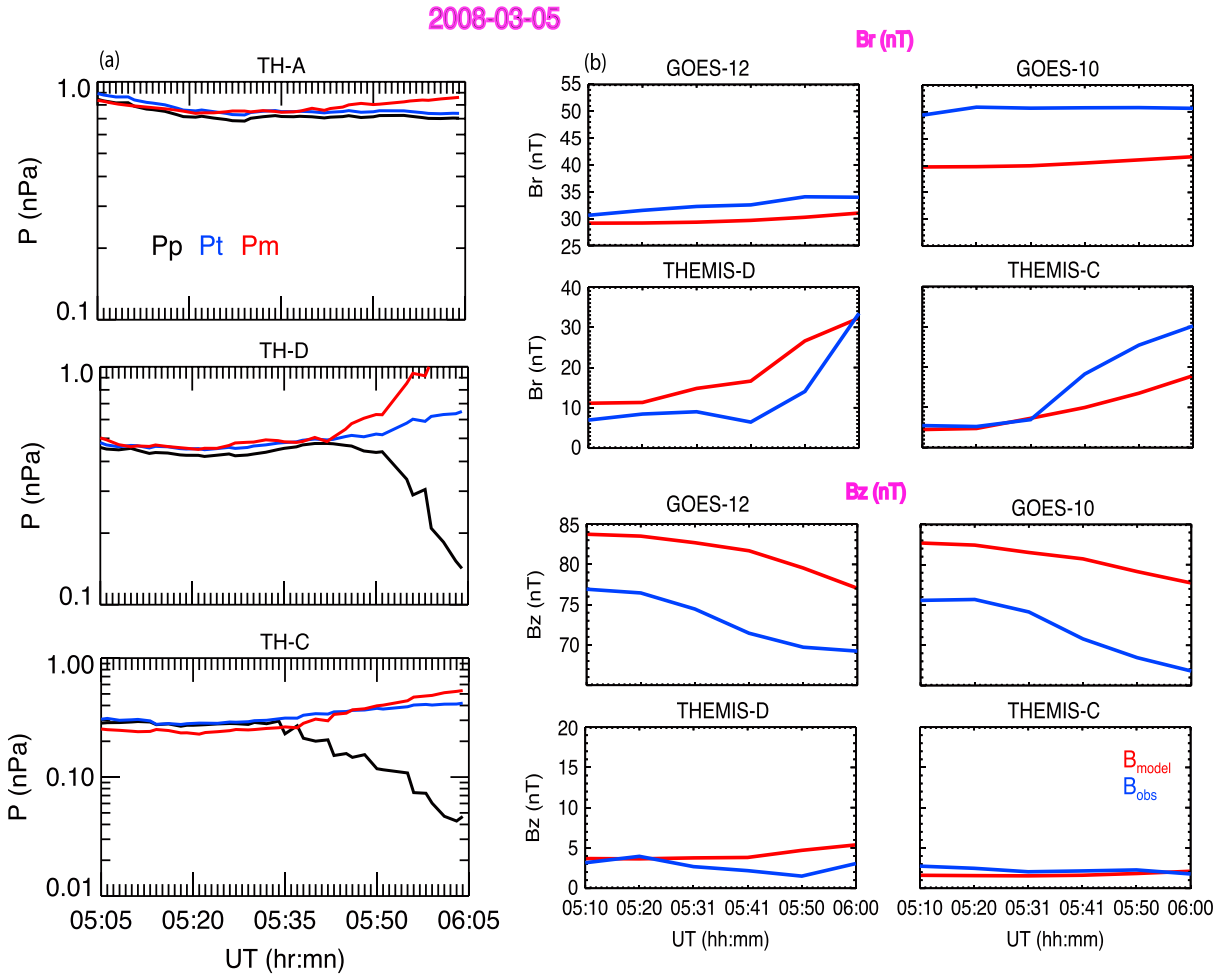

Figure 9. (a) The comparison of the modeled and observed pressures from THEMIS A, D, and C during 05:05–06:05 UT. The black, blue, and red lines are the observed plasma pressure, total pressures, and the modeled pressure, respectively. (b) The magnetic field comparison for geosynchronous GOES 12 and GOES 10 as well as THEMIS D and C satellites from 05:10 to 06:00 UT. The red and blue curves are the model and observation results, respectively. (first and second panels) Magnetic radial B_r component and (third and fourth panels) magnetic B_z component.

In order to evaluate how reliable our modeled magnetic field is for this specific event, Figure 9b compares the model magnetic field B_z component and radial component B_r $\left(B_r = \sqrt{B_x^2 + B_y^2}\right)$ with the observations from GOES 12 and GOES 10, as well as with TH-D and TH-C, during the substorm growth phase from 05:10 to 06:00 UT. Here we have used the GOES satellite-observed magnetic field instead of TH-A because GOES 10 and GOES 12 observed larger B_z than TH-A, indicating that the GOES satellites were likely closer to the central plasma sheet than TH-A. Since we do not know exactly the satellite positions relative to the current sheet, we use the model B_r and B_z at the satellite Z_{GSM} (for GOES) and the observed plasma beta (for THEMIS). Because of this uncertainty in the real Z distance to the current sheet, we focus on comparison of the variation trends but not the exact values. The B_r and B_z comparisons at the different radial locations show that the model magnetic field varies consistently with observed magnetic field variations.

Previous studies have shown that the proton aurora can be used as an excellent indicator for remote sensing certain aspects of magnetotail dynamics [*Samson et al.*, 1992; *Donovan et al.*, 2012] and for testing magnetosphere-ionosphere mapping accuracy [*Ganushkina et al.*, 2005; *Shevchenko et al.*, 2010] since the equatorward boundary of the proton aurora is expected to overlap with the IBs of keV ions due to current sheet scattering under low geomagnetic activity [e.g., *Sergeev et al.*, 2012; *Yue et al.*, 2014]. The low geomagnetic activity during the substorm growth phase of this event (*AE* is smaller than ~100 nT) gives us an excellent opportunity to analyze magnetic field topology change through proton aurora dynamics. Comparing the

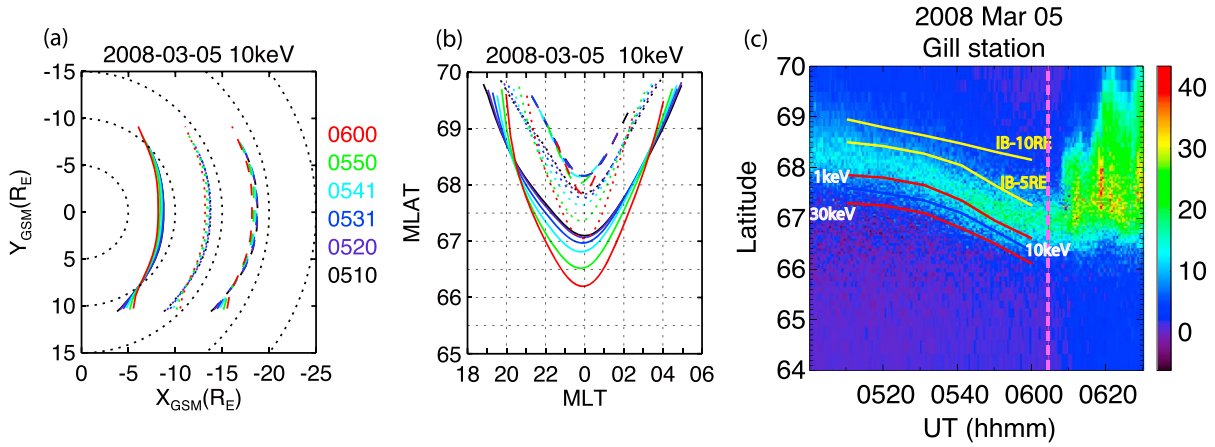

Figure 10. (a) The equatorial ion isotropic boundaries (solid lines), IBs-5 R_E (dot lines), and IBs-10 R_E (dashed lines) in X direction for different time snapshots (black: 05:10 UT; purple: 05:20 UT; blue: 05:31 UT; light blue: 05:41 UT; green: 05:50 UT; red: 06:00 UT) during 5 March 2008 substorm event (onset occurred at 06:04 UT according to auroral observations). (b) The corresponding mapping latitudes in ionosphere as a function of MLT. (c) The proton aurora observations at Gillam station from 05:00 to 06:30 UT. The vertical dashed line marks the substorm onset time. The lower red line, blue line, and the upper red line are the IB latitudes for 30, 10, and 1 keV proton, respectively. The lower and upper yellow lines are the corresponding mapping latitudes for IBs-5 R_E and IBs-10 R_E in X direction.

latitudes of the IBs computed from our model magnetic field with the latitudes of the proton aurora shown in Figure 8b allows us to evaluate the mapping and to understand the equatorward motion of the proton aurora during the growth phase.

Figure 10 shows the computed IBs and their comparisons with the proton aurora. Figures 10a and 10b show the IBs (solid lines) for 10 keV protons at six different times (indicated by different colors) on the equatorial plane and the corresponding latitudes in the ionosphere, respectively. These IBs are calculated from the model 3-D force-balanced magnetic field configurations based on the current sheet scattering criterion (the ratio between the magnetic field curvature radius and the particle gyroradius is less than 8) [*Sergeev et al.*, 1983]. To give a better picture of the mapping under such magnetic field configurations, we also plot in Figures 10a and 10b the equatorial locations that are 5 (dotted lines) and 10 R_E (dashed lines) tailward of the IBs along the X direction and their corresponding ionospheric latitudes, respectively. It can be seen that the IBs are very close to each other on the equatorial plane, with ~0.5 R_E earthward movement near midnight while the IBs in the ionosphere move ~1° equatorward near midnight due to the continuous stretching of magnetic field lines from 05:10 UT to 06:00 UT. It should be noted that our model is not yet able to take into account dipole tilt. However, we have estimated the uncertainty of mapping using the T01 model. The mapping latitude of a point at $X=-9$ and $Y=0$ R_E (approximately the IB locations) at 05:10 UT is ~67.23° when assuming no dipole tilt (current sheet is at $Z=0$) and is ~67.84° when considering dipole tilt (current sheet is at $Z=-0.8$ R_E). This latitude difference is roughly the same throughout the growth phase. So for this event, there is likely a 0.6° uncertainty in latitudes due to the dipole tilt effect. This uncertainty should not affect our results significantly.

It is expected that the earthward edge of the IBs for keV ions should correspond to the equatorward boundary of proton aurora. In Figure 10c, we overplot the evolution of the computed IBs on the proton aurora observed by the 486.1 nm meridian scanning photometer at Gillam. The blue line is the IB evolution for 10 keV proton, while the red lines above and bellow the blue line give the IBs for 1 and 30 keV protons, respectively. It can be seen that the 1 to 30 keV IBs during the growth phase follow very well the equatorward boundary of the proton aurora as it moves equatorward with time. The equatorward motion of the aurora reflects two factors in the model: (1) the continuous stretching of magnetic field lines that map the equatorial IBs to lower latitudes and (2) the movement of Gillam toward midnight where IBs are at lower latitudes than those away from midnight as can be seen in Figure 10b.

The good agreement between the proton aurora and IBs indicates that our model magnetic field reliably represents the realistic growth phase magnetic configuration and its evolution with time. This also indicates that the proton aurora in this event was caused by the current sheet scattering and that the model should give realistic field line mappings from the equator to the ionosphere. As can be seen in the electron aurora shown in

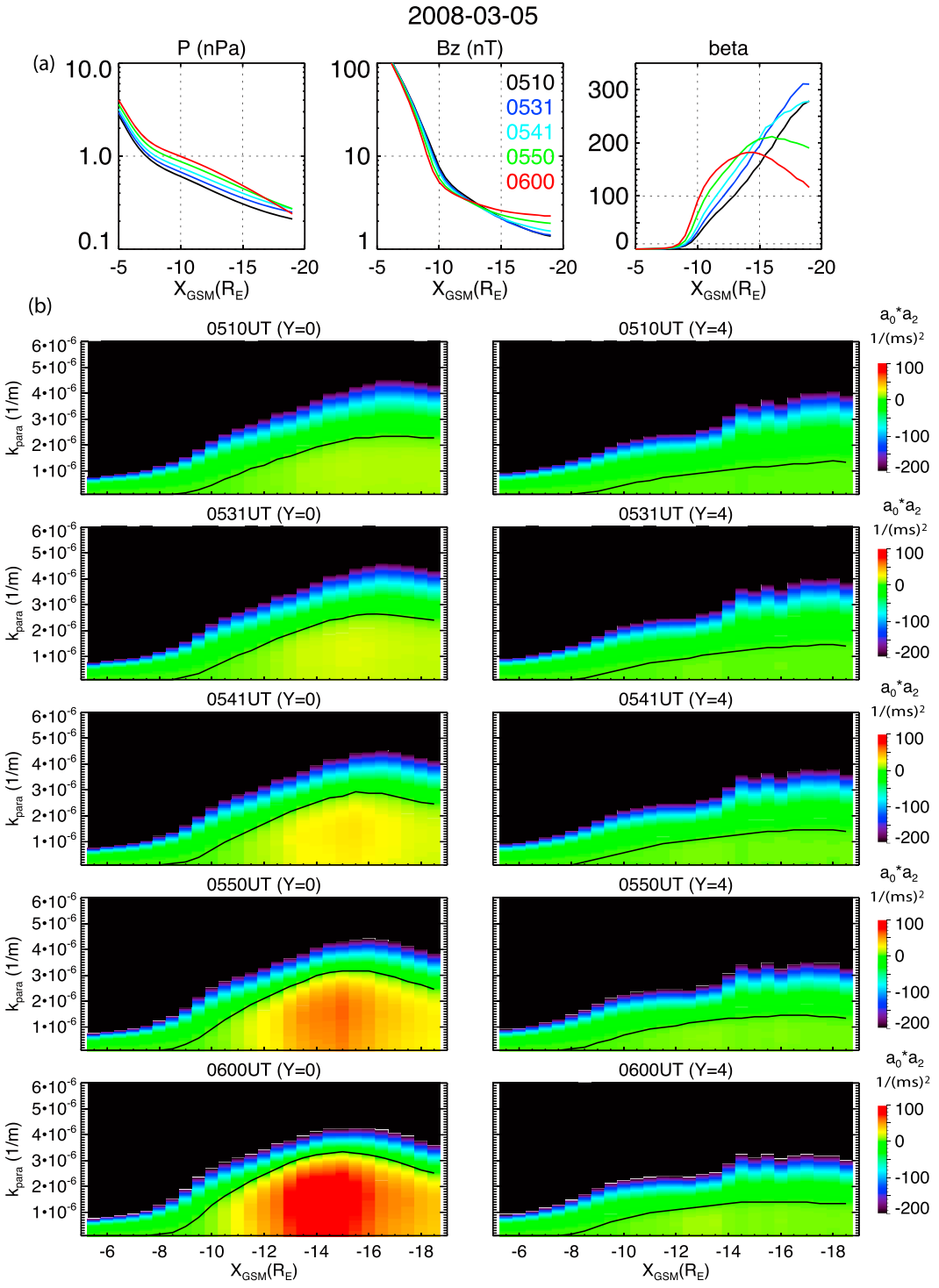

Figure 11. (a) The midnight radial profile of equatorial plasma pressure, B_z, and plasma beta for five different time snapshots during 5 March 2008 substorm event. The black, blue, light blue, green, and red lines are for 05:10, 05:31, 05:41, 05:50, and 06:00 UT, respectively. (b) The equatorial radial profile of equivalent MHD ballooning instability growth rate $a_2 \cdot a_0$ for the same time snapshot as Figure 11a at midnight ($Y = 0$) and $Y = 4$ R_E. The black line marks $a_2 \cdot a_0 = 0$.

Figure 8a, the substorm onset (06:04 UT) started at ~67.3° latitude, which falls between the latitudes of the IB-5 R_E and IB-10 R_E shown in Figure 10c indicated by the two yellow lines. Therefore, we suggest that the substorm onset location in the plasma sheet was at r~14 R_E just before midnight from the magnetic field line mapping.

The ballooning instability occurring during the late growth phase may play a crucial role in leading to the substorm onset. As done in *Xing et al.* [2013], we compute the equivalent MHD ballooning instability growth rate defined in *Pu et al.* [1997] for this substorm event. The second mode of drift ballooning instability (DBI-2) is easy to be triggered when magnetic field line becomes more stretched during the substorm late growth phase. The DBI-2 instability criterion are $a_0 = k_\parallel^2 - \beta k_p k_c < 0$ and $a_2 = 2C_{SL}^2 k_c \left(\frac{k_p}{\gamma} - k_c - k_b\right) - \left(C_A^2 + C_{SL}^2\right)k_\parallel^2 < 0$, and $k_\parallel$ is the parallel wave number. C_A is the Alfvénic velocity and $C_{SL}^2 = C_A^2 C_S^2/\left(C_A^2 + C_S^2\right)$ with C_S being the acoustic speed. Parameter $\gamma = 1$ is the specific heat ratio of isothermal compression. $k_p = \hat{n}\cdot\nabla P/P$, $k_b = \hat{n}\cdot\nabla B/B$, and $k_c = \hat{n}\cdot\left[\left(\hat{b}\cdot\nabla\right)\hat{b}\right]$ are the typical scale lengths of the plasma pressure gradient, magnetic field gradient, and curvature force, respectively.

Figure 11a shows the midnight radial profile of plasma pressure, B_z, and plasma beta for 05:10, 05:31, 05:41, 05:50, and 06:00 UT. The plasma pressure and pressure gradient increase as the substorm growth phase develops, while B_z decreases in the inner magnetosphere and increases in the tail due to the increasing J_φ. Meanwhile, the magnetic field lines become more stretched. No local B_z minimum is formed, but a peak in plasma beta develops after ~05:41 UT. Figure 11b shows the equivalent ballooning instability growth rate $a_2 \cdot a_0$ as functions of radial distance and parallel wave number for five different times at midnight meridian and $Y = 4$ as labeled on top of each panel under the condition that the data with both a_2 and a_0 larger than 0 are not included. By doing this, the positive value of $a_2 \cdot a_0$ indicates that the plasma sheet satisfies the condition of MHD ballooning unstable. We select the range of parallel wave numbers to include the value where the equivalent growth rate becomes zero. The superposed black line indicates the threshold of instability, $a_2 \cdot a_0 = 0$. The DBI-2 mode is found to be unstable for parallel wave numbers smaller than $3.5 \times 10^{-6}\,\mathrm{m}^{-1}$ during the late growth phase around midnight.

As pointed out by *Xing et al.* [2013], a wide range of parallel wavelength may couple to the DBI-2 mode, but the ionosphere may only respond to the lowest parallel wavelength disturbances associated with more intense FACs. In this event, the changes in pressure and magnetic field with increasing energy loading shown in Figure 11a result in larger FACs during the late growth phase, thus providing a condition more favorable to ballooning instability. In addition, the growth rate peaks around r~13–15 R_E at midnight during the late growth phase, which is consistent with the location of the substorm onset derived from the aurora observation in Figure 10.

Previous studies [e.g., *Pritchett and Coroniti*, 2010; *Zhu et al*., 2009] have argued that the ballooning instability is more favorable when there is a B_z minimum in high plasma beta. However, in this event, no B_z minimum is associated with the increasing growth rate of DBI-2 ballooning instability and the maximum growth rate is found to be at the localized peak of plasma beta.

7. Summary and Conclusion

In order to understand evolution of plasma pressure and magnetic field configurations in the plasma sheet ($r \leq 20\ R_E$) and their responses to P_{sw} and sunspot number during the substorm growth phase, we have developed the very first empirical 3-D force-balanced substorm growth phase magnetic field model. We have analyzed the growth phase evolution and evaluated the model predictions. Additionally, we have applied our models to one substorm event to analyze the underlying physical processes and onset location. Major results from this study are

1. The force-balanced substorm growth phase magnetic field model reproduces qualitatively the typical signatures during substorm growth phase. As the substorm growth phase develops (energy loading increases), plasma pressure, pressure gradient, and J_φ increase, while B_{xy} increases off the equator and the equatorial magnetic field B_z decreases in the near-Earth region and increases in the tail due to increasing J_φ. As a result, magnetic field lines become more stretched. J_φ at a given X-Y location peaks off the equator in the near-Earth region, and its peak moves toward equator due to the continuous stretching of magnetic field lines, indicating current sheet thinning as the growth phase develops.

2. The overall model B_z and total magnetic field strength are quantitatively consistent with observations, indicating that our 3-D substorm growth phase magnetic field model performs reasonably well.
3. There are typical Region 1 FACs around r~12 to 20 R_E at the beginning of the substorm growth phase, and they gradually evolve to Region 2 FACs during the late growth phase with their earthward boundary moving to smaller r. The large-scale patterns of the model FACs predicted for a substorm event are quite consistent with the observed FACs from AMPERE, with both showing that FACs intensify as the substorm growth phase develops.
4. The sunspot number effect is nonlinear, and its effect maximizes at sunspot number ~60–80. Compared with the growth phase for a sunspot number of $<$20, the pressure for sunspot number of $<$50 is higher in the inner magnetosphere but lower in the tail, and the magnetic field configuration is slightly more stretched. On the other hand, the P_{sw} effect is linear, and magnetic field lines are found to be significantly more stretched when P_{sw} increases from 2 to 4 nPa.
5. By applying our model to a substorm event, we found that the equatorward movement of proton aurora is mainly associated with the continuous stretching of magnetic field lines during the substorm growth phase, and the ballooning instability in plasma sheet is more favorable around midnight during the late growth phase at the location where there is a local peak in plasma beta. Also, the equatorial mapping of the electron breakup arc for this event is at ~14 R_E before midnight, coinciding with the location of the maximum growth rate for ballooning instability.

The above results show that our modeling can now provide the substorm community a valuable tool to investigate many growth phase physical processes in the plasma sheet, as well as their connection to the ionosphere phenomena. In our future studies, we will continue to apply our methodology to study more substorm events to further verify our conclusions on the ballooning instability and onset locations obtained from this even study.

Acknowledgments

The work by C. Yue, C.-P. Wang, and L.R. Lyons at UCLA has been supported by NASA grants NNX11AJ12G and NNX08A135G, NSF grant ATM-1003595, and IGPPS Program at Los Alamos National Laboratory. We also acknowledge James Weygand (University of California, Los Angeles, USA) for the very helpful discussion of the observed FACs. All THEMIS data are from THEMIS official website (http://themis.ssl.berkeley.edu/data_files.shtml). All Geotail data are from the Institute of Space and Astronautical Science (ISAS)/Japan Aerospace Exploration Agency through the Data Archives and Transmission System of ISAS (http://www.darts.isas.jaxa.jp/).

Michael Liemohn thanks the reviewers for their assistance in evaluating this paper.

References

Anderson, B. J., K. Takahashi, and B. A. Toth (2000), Sensing global Birkeland currents with Iridium® engineering magnetometer data, *Geophys. Res. Lett.*, *27*, 4045–4048, doi:10.1029/2000GL000094.

Angelopoulos, V., C. F. Kennel, F. V. Coroniti, R. Pellat, M. G. Kivelson, R. J. Walker, C. T. Russell, W. Baumjohann, W. C. Feldman, and J. T. Gosling (1994), Statistical characteristics of bursty bulk flow events, *J. Geophys. Res.*, *99*, 21,257–21,280, doi:10.1029/94JA01263.

Angelopoulos, V., et al. (2008), Tail reconnection triggering substorm onset, *Science*, *321*(5891), 931–935.

Auster, H. U., et al. (2008), The THEMIS Fluxgate Magnetometer, *Space Sci. Rev.*, *141*, 235–264, doi:10.1007/s11214-008-9365-9.

Baker, D. N., T. I. Pulkkinen, V. Angelopoulos, W. Baumjohann, and R. L. McPherron (1996), Neutral line model of substorms: Past results and present view, *J. Geophys. Res.*, *101*, 12,975–13,010, doi:10.1029/95JA03753.

Cheng, C. Z., and A. T. Y. Lui (1998), Kinetic ballooning instability for substorm onset and current disruption observed by AMPTE/CCE, *Geophys. Res. Lett.*, *25*, 4091–4094, doi:10.1029/1998GL900093.

Cheng, C. Z., and Q. Qian (1994), Theory of ballooning-mirror instabilities for anisotropic pressure plasmas in the magnetosphere, *J. Geophys. Res.*, *99*, 11,193–11,209, doi:10.1029/94JA00657.

Chu, X., R. L. McPherron, T.-S. Hsu, V. Angelopoulos, Z. Pu, Z. Yao, H. Zhang, and M. Connors (2015), Magnetic mapping effects of substorm currents leading to auroral poleward expansion and equatorward retreat, *J. Geophys. Res. Space Physics*, *120*, 253–265, doi:10.1002/2014JA020596.

Chu, X. N., et al. (2014), Development and validation of inversion technique for substorm current wedge using ground magnetic field data, *J. Geophys. Res. Space Physics*, *119*, 1909–1924, doi:10.1002/2013JA019185.

Donovan, E., et al. (2006), The THEMIS all-sky imaging array-system design and initial results from the prototype imager, *J. Atmos. Sol. Terr. Phys.*, *68*, 1472–1487.

Donovan, E., E. Spanswick, J. Liang, J. Grant, B. Jackel, and M. Greffen (2012), Magnetospheric dynamics and the proton aurora, in *Auroral Phenomenology and Magnetospheric Processes: Earth and Other Planets*, pp. 365–378, AGU, Washington, D. C.

Ganushkina, N. Y., T. I. Pulkkinen, M. V. Kubyshkina, V. A. Sergeev, E. A. Lvova, T. A. Yahnina, A. G. Yahnin, and T. Fritz (2005), Proton isotropy boundaries as measured on mid- and low-altitude satellites, *Ann. Geophys.*, *23*(5), 1839–1847.

Hurricane, O. A. (1997), MHD ballooning stability of a sheared plasma sheet, *J. Geophys. Res.*, *102*, 19,903–19,911, doi:10.1029/97JA01595.

Jiang, F., R. J. Strangeway, M. G. Kivelson, J. M. Weygand, R. J. Walker, K. K. Khurana, Y. Nishimura, V. Angelopoulos, and E. Donovan (2012), In situ observations of the "preexisting auroral arc" by THEMIS all sky imagers and the FAST spacecraft, *J. Geophys. Res.*, *117*, A05211, doi:10.1029/2011JA017128.

Kubyshkina, M., V. Sergeev, N. Tsyganenko, V. Angelopoulos, A. Runov, E. Donovan, H. Singer, U. Auster, and W. Baumjohann (2011), Time-dependent magnetospheric configuration and breakup mapping during a substorm, *J. Geophys. Res.*, *116*, A00I27, doi:10.1029/2010JA015882.

Lee, D. Y., and R. A. Wolf (1992), Is the Earth's magnetotail balloon unstable?, *J. Geophys. Res.*, *97*, 19,251–19,257, doi:10.1029/92JA00875.

Lui, A. T. Y. (1996), Current disruption in the Earth's magnetosphere: Observations and models, *J. Geophys. Res.*, *101*, 13,067–13,088, doi:10.1029/96JA00079.

McCollough, J. P., J. L. Gannon, D. N. Baker, and M. Gehmeyr (2008), A statistical comparison of commonly used external magnetic field models, *Space Weather*, *6*, S10001, doi:10.1029/2008SW000391.

Murphy, K. R., I. R. Mann, I. J. Rae, C. L. Waters, B. J. Anderson, D. K. Milling, H. J. Singer, and H. Korth (2012), Reduction in field-aligned currents preceding and local to auroral substorm onset, *Geophys. Res. Lett.*, *39*, L15106, doi:10.1029/2012GL052798.

Nishimura, Y., et al. (2010), Pre-onset time sequence of auroral substorms: Coordinated observations by all-sky imagers, satellites and radars, *J. Geophys. Res.*, *115*, A00I08, doi:10.1029/2010JA015832.

Olson, W. P., and K. A. Pfitzer (1974), Quantitative model of magnetospheric magnetic field, *J. Geophys. Res.*, *79*, 3739–3748, doi:10.1029/JA079i025p03739.

Pritchett, P. L., and F. V. Coroniti (2010), A kinetic ballooning/interchange instability in the magnetotail, *J. Geophys. Res.*, *115*, A06301, doi:10.1029/2009JA014752.

Pu, Z. Y., A. Korth, Z. X. Chen, R. H. W. Friedel, Q. G. Zong, X. M. Wang, M. H. Wong, S. Y. Fu, and T. I. Pulkkinen (1997), MHD drift ballooning instability near the inner edge of the near-Earth plasma sheet, *J. Geophys. Res.*, *102*, 14,397–14,406, doi:10.1029/97JA00772.

Saito, M. H., L.-N. Hau, C.-C. Hung, Y.-T. Lai, and Y.-C. Chou (2010), Spatial profile of magnetic field in the near-Earth plasma sheet prior to dipolarization by THEMIS: Feature of minimum B, *Geophys. Res. Lett.*, *37*, L08106, doi:10.1029/2010GL042813.

Saito, M. H., D. Fairfield, G. Le, L.-N. Hau, V. Angelopoulos, J. P. McFadden, U. Auster, J. W. Bonnell, and D. Larson (2011), Structure, force balance, and evolution of incompressible cross-tail current sheet thinning, *J. Geophys. Res.*, *116*, A10217, doi:10.1029/2011JA016654.

Samson, J. C., L. R. Lyons, P. T. Newell, F. Creutzberg, and B. Xu (1992), Proton aurora and substorm intensifications, *Geophys. Res. Lett.*, *19*, 2167–2170, doi:10.1029/92GL02184.

Sergeev, V., Y. Nishimura, M. Kubyshkina, V. Angelopoulos, R. Nakamura, and H. Singer (2012), Magnetospheric location of the equatorward prebreakup arc, *J. Geophys. Res.*, *117*, A01212, doi:10.1029/2011JA017154.

Sergeev, V. A., E. M. Sazhina, N. A. Tsyganenko, J. A. Lunbland, and F. Soraas (1983), Pitch angle scattering of energetic protons in the magnetotail current sheet as the dominant source of their isotropic precipitation into the nightside ionosphere, *Planet. Space Sci.*, *31*, 1147–1158.

Shevchenko, I. G., V. Sergeev, M. Kubyshkina, V. Angelopoulos, K. H. Glassmeier, and H. J. Singer (2010), Estimation of magnetosphere-ionosphere mapping accuracy using isotropy boundary and THEMIS observations, *J. Geophys. Res.*, *115*, A11206, doi:10.1029/2010JA015354.

Shiokawa, K., W. Baumjohann, and G. Haerendel (1997), Braking of high speed flows in the near-Earth tail, *Geophys. Res. Lett.*, *24*, 1179–1182, doi:10.1029/97GL01062.

Singer, H., L. Matheson, R. Grubb, A. Newman, and D. Bouwer (1996), Monitoring space weather with the GOES magnetometers, in *GOES-8 and Beyond*, vol. 2812, edited by E. R. Washwell, pp. 299–308, Soc. of Photogr. Instrum. Eng., Bellingham, Wash.

Tsyganenko, N. A. (1995), Modeling the Earth's magnetospheric magnetic field confined within a realistic magnetopause, *J. Geophys. Res.*, *100*, 5599–5612, doi:10.1029/94JA03193.

Tsyganenko, N. A. (1996), Effects of the solar wind conditions on the global magnetospheric configuration as deduced from data-based field models, in *Proceedings of the ICS-3 Conference on Substorms*, *Eur. Space Agency Spec. Publ.*, vol. 389, pp. 181–185, Eur. Space Agency, Noordwijk, Netherlands.

Vasyliunas, V. M. (1970), Mathematical models of magnetospheric convection and its coupling to the ionosphere, in *Particles and Fields in the Magnetosphere*, edited by B. M. McCormac, pp. 60–71, D. Reidel, Hingham, Mass.

Vasyliunas, V. M. (1984), Fundamentals of current description, in *Magnetospheric Currents*, *Geophys. Monogr. Ser.*, vol. 28, edited by T. A. Potemra, pp. 63–66, AGU, Washington, D. C.

Voigt, G.-H., and R. A. Wolf (1988), Quasi-static magnetospheric MHD processes and the "ground state" of the magnetosphere, *Rev. Geophys.*, *26*, 823–843, doi:10.1029/RG026i004p00823.

Wang, C.-P., L. R. Lyons, R. A. Wolf, T. Nagai, J. M. Weygand, and A. T. Y. Lui (2009), The plasma sheet PV5/3 and nV and associated plasma and energy transport for different convection strengths and *AE* levels, *J. Geophys. Res.*, *114*, A00D02, doi:10.1029/2008JA013849.

Waters, C. L., B. J. Anderson, and K. Liou (2001), Estimation of global field aligned currents using the Iridium® system magnetometer data, *Geophys. Res. Lett.*, *28*, 2165–2168, doi:10.1029/2000GL012725.

Xing, X., and R. A. Wolf (2007), Criterion for interchange instability in a plasma connected to a conducting ionosphere, *J. Geophys. Res.*, *112*, A12209, doi:10.1029/2007JA012535.

Xing, X., J. Liang, E. Spanswick, L. Lyons, and V. Angelopoulos (2013), Auroral wave structures and ballooning instabilities in the plasma sheet, *J. Geophys. Res. Space Physics*, *118*, 6319–6326, doi:10.1002/2013JA019068.

Yue, C., C.-P. Wang, S. G. Zaharia, X. Xing, and L. Lyons (2013), Empirical modeling of plasma sheet pressure and three-dimensional force-balanced magnetospheric magnetic field structure: 2. Modeling, *J. Geophys. Res. Space Physics*, *118*, 6166–6175, doi:10.1002/2013JA018943.

Yue, C., C.-P. Wang, L. Lyons, J. Liang, E. F. Donovan, S. G. Zaharia, and M. Henderson (2014), Current sheet scattering and ion isotropic boundary under 3-D empirical force-balanced magnetic field, *J. Geophys. Res. Space Physics*, *119*, 8202–8211, doi:10.1002/2014JA020172.

Yue, C., C.-P. Wang, L. Lyons, Y. Wang, T. Hsu, M. Henderson, A. T. Y. Lui, V. Angelopoulos, and T. Nagai (2015), A 2D empirical plasma sheet pressure model for substorm growth phase using the Support Vector Regression Machine, *J. Geophys. Res. Space Physics*, *120*, 1957–1973, doi:10.1002/2014JA020787.

Zaharia, S. (2008), Improved Euler potential method for three-dimensional magnetospheric equilibrium, *J. Geophys. Res.*, *113*, A08221, doi:10.1029/2008JA013325.

Zaharia, S., and C. Z. Cheng (2003), Can an isotropic plasma pressure distribution be in force balance with the T96 model field?, *J. Geophys. Res.*, *108*(A11), 1412, doi:10.1029/2002JA009501.

Zhu, P., J. Raeder, K. Germaschewski, and C. C. Hegna (2009), Initiation of ballooning instability in the near-Earth plasma sheet prior to the 23 March 2007 THEMIS substorm expansion onset, *Ann. Geophys.*, *27*(3), 1129–1138.